An Equivalent Current Source Model and Laplacian Weighted Minimum Norm Current Estimates of Brain Electrical Activity

Bin He*, *Senior Member, IEEE*, D. Yao, Jie Lian, *Student Member, IEEE*, and D Wu

***Abstract*—We have developed a method for estimating the three-dimensional distribution of equivalent current sources inside the brain from scalp potentials. Laplacian weighted minimum norm algorithm has been used in the present study to estimate the inverse solutions. A three-concentric-sphere inhomogeneous head model was used to represent the head volume conductor. A closed-form solution of the electrical potential over the scalp and inside the brain due to a point current source was developed for the three-concentric-sphere inhomogeneous head model. Computer simulation studies were conducted to validate the proposed equivalent current source imaging. Assuming source configurations as either multiple dipoles or point current sources/sinks, in computer simulations we used our method to reconstruct these sources, and compared with the equivalent dipole source imaging. Human experimental studies were also conducted and the equivalent current source imaging was performed on the visual evoked potential data. These results highlight the advantages of the equivalent current source imaging and suggest that it may become an alternative approach to imaging spatially distributed current sources-sinks in the brain and other organ systems.**

***Index Terms*—Brain electric source imaging, equivalent current source, equivalent dipole source, forward problem, high-resolution EEG, inverse problem.**

I. Introduction

BRAIN electrical activity is spatially distributed over three dimensions of the brain and evolves with time. It is of significance and importance to image brain electrical activity from the noninvasive scalp electroencephalogram (EEG). A significant amount of effort has been put forth in the past decades in the development of high-resolution EEG-based source-imaging techniques, which attempt to image spatially distributed brain electrical activity without *ad hoc* assumption on the number of source dipoles [1], [2]. Due to the high temporal resolution inherent in the EEG, the availability of EEG-based source-imaging modalities provides much needed high temporal resolution in mapping the functional status of the brain, as well as low cost of EEG procedures as compared with other imaging modalities.

Different source models have been investigated to image the brain electrical sources, and two major categories are *dipole localization* and *distributed source imaging*. The early approach in dipole localization is to search for a single or a few dipoles whose forward solutions can best fit the scalp potential measurement [3]–[5]. The multiple-signal classification (MUSIC) algorithm was further applied to the brain inverse problem, in which the multiple dipole locations are found by scanning potential locations using a simple one dipole model [6]. When dealing with the distributed sources without *ad hoc* knowledge of the number of sources, the distributed source imaging methods are preferred. A popular distributed inverse source solution was the simple *minimum norm* (MN) solution [7], which estimates the three-dimensional (3-D) brain source distribution with the smallest two-norm solution vector that would match the measured data. To compensate for the undesired depth dependency of the original MN solutions, which favors superficial sources, different weighting methods were introduced. The representative approaches include the diagonal matrix *weighted minimum norm* (WMN) solution [8], [9], and the *Laplacian weighted minimum norm* (LWMN) solution [10]–[13]. The WMN compensates for the lower gains of deeper sources by using lead-field normalization, while the LWMN combines the lead-field normalization with the Laplacian operator, thus, gives the depth-compensated inverse solution under the constraint of smoothly distributed sources. Different variants of the MN solution were also proposed, by incorporating *a priori* information as constraint [14], [15], by estimating the source-current covariance matrix from the measured data [16], or by using linear [17] or nonlinear [18] approaches.

The inverse problem of brain source imaging is highly underdetermined in that the number of unknowns is much more than the available sensors. If dipoles are modeled as the distributed sources in N spatial locations, the solution space consists of $3N$ unknown variables in EEG-based source imaging because each dipole has three directional components. On the other hand, only N variables need to be determined if the distributed sources are modeled by the current monopoles, therefore, it has the potential to dramatically simplify the calculation.

Manuscript received May 21, 2001; revised October 31, 2001. This work was supported in part by the National Science Foundation (NSF) under CAREER Award BES-9875344, in part by a grant from the Whitaker Foundation, and in part by a grant from the Campus Research Board of the University of Illinois at Chicago. *Asterisk indicates corresponding author.*

*B. He is with the Department of Bioengineering and the Department of Electrical and Computer Engineering, The University of Illinois at Chicago, M/C-063, 851 S. Morgan Street, Chicago, IL 60607 USA. (e-mail: bhe@uic.edu).

D. Yao was with the Department of Electrical and Computer Engineering, The University of Illinois at Chicago, Chicago, IL 60607 USA. He is now with the University Electronic Science and Technology of China, Chengdu, China.

J. Lian is with the Department of Bioengineering, The University of Illinois at Chicago, Chicago, IL 60607 USA.

D. Wu was with the Department of Bioengineering, The University of Illinois at Chicago, Chicago, IL 60607 USA. She is now with Morningstar Inc. Chicago, IL 60607 USA.

Publisher Item Identifier S 0018-9294(02)02991-9.

Another alternative approach (ELECTRA) to the 3-D brain inverse source imaging is to reconstruct the electrical potential over the 3-D volume of the brain from scalp EEG [46]. The feasibility of estimating the electrical potential in the 3-D brain and merits of reducing the number of unknowns were demonstrated in computer simulations and human visual evoked potential (VEP) experiments [46]. The forward solution of the magnetic fields generated by the current monopoles in spherical and semi-infinite volume conductors was formulated by Ferguson and Durand [19], while the EEG forward theory due to the point current sources in three-sphere head model has not been well established.

In the present study, we have developed a method to estimate brain electric activity throughout the 3-D brain tissues from noninvasive scalp EEGs by means of the equivalent current source model. We have developed the theoretical forward solution of the scalp potentials due to a point current source located inside a three-concentric-sphere inhomogeneous head model, and compared the LWMN-based equivalent-current inverse solution (ECS) with the equivalent-dipole inverse solution (EDS) [10] in both computer simulations and human experimental studies. While the fundamental relationship between the equivalent monopole (and dipole) source density and the resulting electrical potential field has been well established [20], [47], [48], the present work reports, to our knowledge, the first investigation on the feasibility and applicability of estimating the 3-D equivalent neural current source distribution from scalp EEG.

II. Equivalent Current Source Imaging

A. Equivalent Monopole Current Source Model

Under quasistatic conditions, it is well known that the bioelectric potential obeys Possion's equation [20]

$$\nabla^2\Phi = \frac{\nabla\cdot\vec{J^i}}{\sigma} = -\frac{I_v}{\sigma}. \tag{1}$$

Equation (1) is a partial differential equation satisfied by the electrical potential Φ in which I_v is the *source function*. The solution of (1) for the scalar function Φ for a region that is uniform and infinite in extent [20], [21], [47], [48] is

$$\Phi = -\frac{1}{4\pi\sigma}\int_v\left(\frac{1}{r}\right)\nabla\cdot\vec{J^i}dv. \tag{2}$$

Since a source element $\nabla\cdot\vec{J^i}dv$ in (2) behaves like a *point current source*, in that it sets up a field, that varies as $1/r$, the expression $I_v = -\nabla\cdot\vec{J^i}$ can be considered as an *equivalent monopole current source density* [20], [47], [48].

The equivalent current source model we propose is to equivalently represent bioelectric activity by the source function $I_v = -\nabla\cdot\vec{J^i}$. Equations (1) and (2) show that the equivalent current source behaves as a fundamental driving force establishing the electrical potentials inside the brain and over the passive medium of the head volume conductor.

B. Estimation of Equivalent Current Sources

Discretizing (2), the scalp potential vector Φ can be related to the equivalent current source vector $\boldsymbol{X}$ as follows:

$$\Phi = AX \tag{3}$$

where $\Phi = (\phi_1, \phi_2, \ldots, \phi_M)$ and $X = (x_1, x_2, \ldots, x_N)$. M refers to the number of scalp recording electrodes and N refers to the number of the equivalent point current sources. For an inhomogeneous volume conductor, (3) can also be derived using appropriate numerical techniques by solving Poisson's equation (1). The inverse problem, therefore, becomes solving (3) for $\boldsymbol{X}$.

Equation (3) is a heavily underdetermined system because normally $N \gg M$. There are an infinite number of solutions that may satisfy (3). The unique MN solution is one of the feasible solutions [7], [9], [13], [15], [22]

$$X = A^+\Phi = A^T(AA^T)^-\Phi \tag{4}$$

where $(*)^+$ denotes the Moore-Penrose inverse and $(*)^-$ denotes the inverse of $(*)$.

As the MN solution is of an intrinsic bias to the superficial position, a few weighting operators have been introduced [8]–[13]. For the LWMN algorithm (LORETA) [10]–[13], it used a weighting operator LW, where L is a Laplacian operator and W is a diagonal N by N matrix with $w_{ii} = \|A_i\|$, A_i is the ith column of the transfer matrix A. Assuming the weighting factor is nonsingular, we have

$$X = \left(WL^TLW\right)^- A^T\left(A\left(WL^TLW\right)^- A^T\right)^-\Phi. \tag{5}$$

In order to overcome the numerical instability due to the ill-posed nature of the inverse system, regularization is necessary for the matrix inversion in (4) and (5). The Tikhonov regularization and truncated singular-value decomposition (TSVD) are two commonly used regularization methods. Different methods can be applied to determine the regularization parameters (for details, see [23]). In the present study, the TSVD was applied to solve the inverse problem, and the truncation parameter was determined by the discrepancy principle [24], so that the resulting residual norm equals to the norm of the estimated noise in the scalp potential measurement [23], [24].

Note that for the equivalent current source estimate, the number of unknowns in the solution vector X is N, which is one third of that of the equivalent dipole source estimate. This decrease in the solution space dramatically reduces the computation effort involved in (5), because the dimensions of matrices A, W, and L are also decreased, respectively.

C. Simulation Protocols and Forward Model Solutions

In the present study, computer simulations were conducted to validate the proposed ECS imaging approach. Comparison was also made with the EDS imaging approach [10]. As shown in Fig. 1, a concentric three-sphere inhomogeneous head model [25] was used to represent the head volume conductor. The normalized radii of the brain, the skull and the scalp were taken as 0.87, 0.92, and 1.0, respectively [25], [41]. The normalized conductivity of the scalp and the brain was taken as 1.0, and

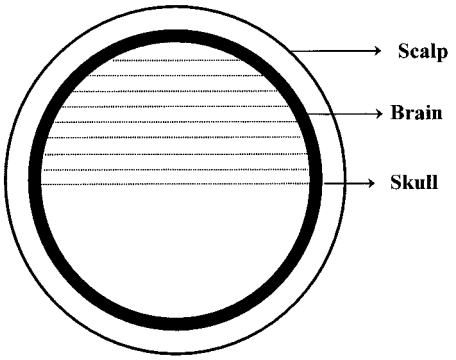

Fig. 1. Illustration of the source-conductor model, used in the present study. The head is represented by an inhomogeneous concentric three-sphere volume conductor model. The dotted lines are a schematic illustration of the solution space, over which the source distributions are illustrated in Fig. 2.

that of the skull as 0.0125 [5], [25]. The 3-D solution space extends from the center of the sphere to an eccentricity of 0.87 of the upper hemisphere. In the present study, solutions were calculated on a discrete cubic grid consisting of $N = 1509$ voxels distributed in nine layers $(z = 0.0, 0.1, \ldots, 0.8)$, with inter-grid distance of 0.1, which gives spatial resolution of 1 cm on a typical spherical head model with radius of 10 cm. Such choice of the grid size is to achieve reasonably high enough resolution considering the limitation of the spatial resolution by the LWMN algorithm. For each voxel, a point current, or three dipoles along the three axes were considered. Therefore, the total unknown quantities were 1509 for the ECS imaging and $3N = 4527$ for the EDS imaging. The number of the scalp electrodes used in the present investigation was $M = 129$, which were uniformly distributed over the upper hemisphere of the head, and represents a desired spatial sampling rate. The transfer matrix from the equivalent point current source to the scalp potential can be found from the formulation described in Section III. Again, the computational advantage of the ECS as compared with the EDS is obvious when considering the dimensions of the matrices in (5).

In the present simulation study, four different source configurations, which represent same basic source configurations of possible multiple sources/sinks, were investigated and illustrated in Fig. 2 as examples. In Fig. 2(a), four radial dipoles located at Cartesian coordinate of $(\pm 0.4, 0, 0.4)$ and $(0, \pm 0.4, 0.4)$ were used to simulate four regions of localized brain activity. The two dipoles located on the x axis were oriented outwards and the two dipoles located on the y axis inwards. Fig. 2(b) illustrates another example of dipole sources in which four tangential dipoles were located at $(\pm 0.4, 0, 0.4)$ and $(0, \pm 0.4, 0.4)$, all pointing counter-clockwise. Fig. 2(c) illustrates an example of four point current sources/sinks located at $(\pm 0.4, 0, 0.4)$ and $(0, \pm 0.4, 0.4)$. The two on the x axis were current sources (with positive signs) and the two on the y axis were the current-sinks (with negative signs). In Fig. 2(d), a point current source (with positive sign) located at (0.4, 0, 0.4) and a point current sink (with negative sign) located at (0, 0.4, 0.4) were used to simulate a source/sink configuration of brain electrical activity.

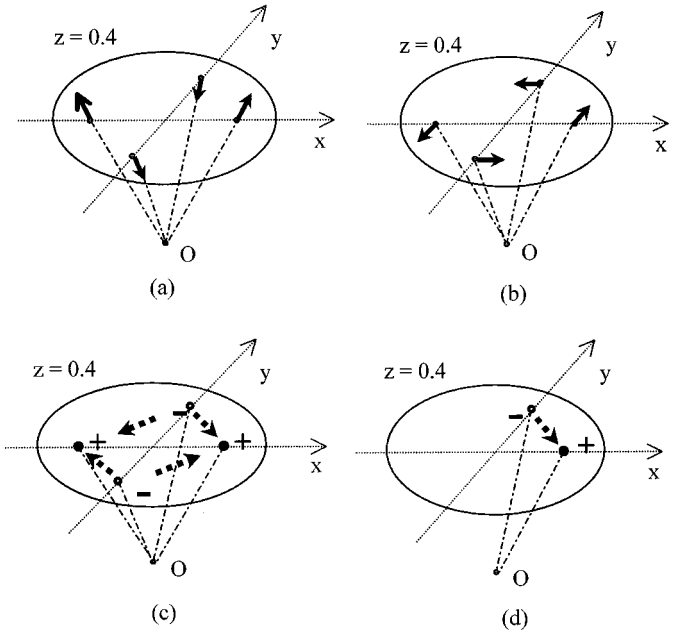

Fig. 2. Illustration of the simulated source configurations. (a) Four radial dipoles. (b) Four tangential dipole. (c) Two-point current sources and two-point current sinks. (d) One pair of point current source/sink. (See text for details.)

For all the simulated source configurations, the scalp potential generated by the assumed electrical sources were calculated analytically (see Section III). Gaussian white noise (GWN) of 10% was added to the calculated scalp potentials to simulate the noise-contaminated scalp potentials. The noise level is defined as the ratio between the standard deviation of GWN and the standard deviation of the simulated scalp potential over all electrodes. The 10% noise level was selected since it represents a typical noise level for EEG signals. Both ECS imaging and EDS imaging were conducted to inversely estimate the 3-D electrical source distribution.

D. Human VEP Experimentation

Visual evoked potential (VEP) experiments were conducted in human subjects to evaluate the performance of the proposed ECS imaging approach. Comparison was also made with the EDS imaging approach [10]. Two healthy subjects who gave written informed consent were studied in accordance with a protocol approved by the UIC/IRB. Visual stimuli were generated by the STIM system (Neuro Scan Labs). 94-channel VEP signals referenced to right earlobe were amplified with a gain of 500 and band pass filtered from 1 Hz to 200 Hz by Synamps (Neuro Scan Labs), and were acquired at a sampling rate of 1 kHz by using SCAN 4.1 software (Neuro Scan Labs). The electrode locations were measured using Polhemus Fastrack (Polhemus Inc.) and best fitted on the spherical surface with unit radius. Half visual field pattern reversal checkerboards (black and white) with reversal frequency of 2 Hz served as visual stimuli and 300 reversals were recorded to obtain averaged VEP signals. The display had a total viewing angle of 14.3° by 11.1°, and the checksize was set to be $175'$ by $135'$ expressed in arc minutes.

III. Scalp Potentials Generated by a Point Current Source in a Three-Concentric Spheres Head Model

In this section we derive the forward solutions of the potentials on the scalp and inside the brain by a point current source in a three-concentric-sphere head model [25]. While the solutions of the potential due to a dipole source are previously available [26], [27], we present the derivation of the potential by both a dipole current and a point current source in a unified way.

The potential distribution of an arbitrarily positioned and orientated dipole in an infinite medium is given by [21]

$$\begin{aligned}\Phi_\infty =&\frac{1}{4\pi\sigma}\vec{P}\cdot\nabla_{r_0}\left(\frac{1}{r_p}\right)\\ =&\frac{1}{4\pi\sigma}\left\{P_r\frac{\partial}{\partial r_0}+P_\varphi\frac{1}{r_0\sin\theta_0}\frac{\partial}{\partial\varphi_0}+P_\theta\frac{1}{r_0}\frac{\partial}{\partial\theta_0}\right\}\frac{1}{r_p}\end{aligned} \tag{6}$$

where $\vec{P}$ is the dipole vector with components of $(P_r, P_\varphi, P_\theta)$ in spherical coordinate system. For a point current source in an infinite medium, the potential is given by

$$\Phi_\infty = \frac{1}{4\pi\sigma}\frac{I}{r_p} \tag{7}$$

where, I is the current source strength. Using the associated Legendre function, we can obtain [28],

$$\begin{aligned}\frac{1}{r_p} =&\sum_{l=0}^{\infty}\sum_{m=0}^{l}\frac{r_0^l}{r^{l+1}}\left(2-\delta_m^0\right)\frac{(l-m)!}{(l+m)!}P_l^m(\cos\theta_0)\\ &\times P_l^m(\cos\theta)\cos m(\varphi-\varphi_0)\end{aligned} \tag{8}$$

$$\begin{aligned}\frac{\partial P_l^m}{\partial\theta_0} =&-\frac{1}{2}\left[(l-m+1)(l+m)P_l^{m-1}(\cos\theta_0)\right.\\ &\left.-P_l^{m+1}(\cos\theta_0)\right]\end{aligned} \tag{9}$$

and

$$\frac{\partial P_l}{\partial\theta_0} = P_l^1(\cos\theta_0) \tag{9a}$$

where $\delta_m^0 = 1$ when $m = 0$, and $\delta_m^0 = 0$ when $m \neq 0$, and $(r_0, \theta_0, \varphi_0)$ and (r, θ, φ) are the standard spherical coordinates of the source position and field point, r_p is the distance from the source point to the field point, P_n^m is the associated Legendre function of the first kind. From (8), (9), and (9a), (6) can be rewritten as

$$\begin{aligned}\Phi_\infty =&\sum_{l=1}^{\infty}\sum_{m=0}^{l}\frac{K_l^m(\vec{P})}{r^{l+1}}\left(H_l^m\cos m\varphi+G_l^m\sin m\varphi\right)\\ &\times P_l^{m+1}(\cos\theta)\\ =&\sum_{l=1}^{\infty}\sum_{m=0}^{l}\frac{K_l^m(\vec{P})}{r^{l+1}}S_l^m(\vec{P},\theta,\varphi)\end{aligned} \tag{10}$$

where

$$S_l^m(\vec{P},\theta,\varphi) = \left(H_l^m\cos m\varphi+G_l^m\sin m\varphi\right)P_l^m(\cos\theta) \tag{10a}$$

$$K_l^m(\vec{P}) = \frac{r_0^{l-1}}{4\pi\sigma}\left(2-\delta_m^0\right)\frac{(l-m)!}{(l+m)!} \tag{10b}$$

$$\begin{aligned}H_l^m =&lP_rP_l^m(\cos\theta_0)\cos m\varphi_0\\ &-\frac{mP_\varphi}{\sin\theta_0}P_l^m(\cos\theta_0)\sin m\varphi_0\\ &-\frac{P_\theta}{2}\left((l-m+1)(l+m)\right.\\ &\left.\times P_l^m(\cos\theta_0)-P_l^{m+1}(\cos\theta_0)\right)\\ &\times\cos m\varphi_0\\ G_l^m =&lP_rP_l^m(\cos\theta_0)\sin m\varphi_0\\ &+\frac{mP_\varphi}{\sin\theta_0}P_l^m(\cos\theta_0)\cos m\varphi_0\\ &-\frac{P_\theta}{2}\left((l-m+1)(l+m)P_l^{m-1}(\cos\theta_0)\right.\\ &\left.-P_l^{m+1}(\cos\theta_0)\right)\sin m\varphi_0\end{aligned}$$

and (7) changes to

$$\begin{aligned}\Phi_\infty =&\sum_{l=1}^{\infty}\sum_{m=0}^{l}\frac{K_l^m(I)}{r^{l+1}}(\cos m\varphi_0\cos m\varphi+\sin m\varphi_0\sin m\varphi)\\ &\times P_l^m(\cos\theta_0)P_l^m(\cos\theta)\\ =&\sum_{l=1}^{\infty}\sum_{m=0}^{l}\frac{K_l^m(I)}{r^{l+1}}S_l^m(I,\theta,\varphi)\end{aligned} \tag{11}$$

where

$$\begin{aligned}S_l^m(I,\theta,\varphi) =&(\cos m\varphi_0\cos m\varphi+\sin m\varphi_0\sin m\varphi)\\ &\times P_l^m(\cos\theta_0)P_l^m(\cos\theta)\end{aligned} \tag{11a}$$

$$K_l^m(I) = \frac{Ir_0^l}{4\pi\sigma}\left(2-\delta_m^0\right)\frac{(l-m)!}{(l+m)!}. \tag{11b}$$

Note that the index l starts from one in (10) instead of zero as in (8), since the term corresponding to $l = 0$ is zero. In (11), the $l = 0$ term was omitted due to the electrical neutrality for a living system that requires the total sum of the currents inside a living system vanishes.

In the above equations, $S_l^m(\vec{P},\theta,\varphi)$ is determined by the dipole position and moment, and has no relation to the radial variable r. $K_l^m(\vec{P})$ is a constant which is totally determined by the dipole. $S_l^m(I,\theta,\varphi)$ is determined by the point current source position and its strength, and has no relation to the radial variable r, and $K_l^m(I)$ is a constant which is totally determined by the point current source. Because of the similarity between (10) and (11), a general formula is given below, in order to simplify the following derivation.

$$\Phi_\infty = \sum_{l,m}\frac{K_l^m}{r^{l+1}}S_l^m(\theta,\varphi). \tag{12}$$

For a dipole source, $K_l^m = K_l^m(\vec{P})$, $S_l^m(\theta,\varphi) = S_l^m(\vec{P},\theta,\varphi)$; while for a point current source, $K_l^m = K_l^m(I)$ and $S_l^m(\theta,\varphi) = S_l^m(I,\theta,\varphi)$. We will not specify them in the following derivation for the sake of simplicity.

As the boundary condition requires that the potential is continuous across the boundary, which is shown by the following (14) and (14b), for a concentric multi-sphere conductive medium, $S_l^m(\theta,\varphi)$ may be chosen as the common basic function form for each sub-region. Based on (10) and (11), the

expression of the potential in the inner sphere can be assumed to be the following:

$$\Phi_1 = \sum_{l,m} \left[A_l^m r^l + K_l^m \frac{1}{r^{l+1}} \right] S_l^m. \tag{13}$$

In the second and third layers, the potentials are expressed as the solution of Laplace's equation

$$\Phi_2 = \sum_{l,m} \left[C_l^m r^l + D_l^m \frac{1}{r^{l+1}} \right] S_l^m \tag{13a}$$

$$\Phi_3 = \sum_{l,m} \left[E_l^m r^l + F_l^m \frac{1}{r^{l+1}} \right] S_l^m. \tag{13b}$$

The boundary conditions are

$$\Phi_1 = \Phi_2|_{r=a} \tag{14}$$

$$\sigma_1 \frac{\partial \Phi_1}{\partial r} = \sigma_2 \frac{\partial \Phi_2}{\partial r}\bigg|_{r=a} \tag{14a}$$

$$\Phi_3 = \Phi_2|_{r=b} \tag{14b}$$

$$\sigma_3 \frac{\partial \Phi_3}{\partial r} = \sigma_2 \frac{\partial \Phi_2}{\partial r}\bigg|_{r=b} \tag{14c}$$

$$\frac{\partial \Phi_3}{\partial r} = 0|_{r=c}. \tag{14d}$$

In the above, σ_1, σ_2 and σ_3 refer to the conductivities for the brain tissue, the skull, and the scalp, respectively, a, b, and c refer to the radii of the three spheres. The boundary conditon (14) implies

$$C_l^m a^l + D_l^m \frac{1}{a^{l+1}} = A_l^m a^l + K_l^m \frac{1}{a^{l+1}}. \tag{15}$$

The boundary condition (14d) yields

$$E_l^m l c^{l-1} - F_l^m (l+1) \frac{1}{c^{l+2}} = 0 \tag{15a}$$

or

$$E_l^m = F_l^m \frac{l+1}{l} \frac{1}{c^{2l+1}}. \tag{15b}$$

From the boundary condition (14b) we have

$$C_l^m b^l + D_l^m \frac{1}{b^{l+1}} = F_l^m \left(b^l \frac{l+1}{l} c^{-(2l+1)} + b^{-(l+1)} \right) \tag{15c}$$

and the boundary condition (14c) results in

$$\sigma_2 \left[C_l^m l b^{l-1} - D_l^m (l+1) \frac{1}{b^{l+2}} \right] = \sigma_3 F_l^m (l+1) \left[b^{l-1} c^{-(2l+1)} - \frac{1}{b^{l+2}} \right]. \tag{15d}$$

Equating F_l^m from the above two equations we find

$$\frac{C_l^m b^{2l+1} + D_l^m}{\left(\frac{b}{c}\right)^{2l+1} \frac{l+1}{l} + 1} = \frac{\sigma_2}{\sigma_3} \frac{C_l^m \frac{l}{l+1} b^{2l+1} - D_l^m}{\left(\frac{b}{c}\right)^{2l+1} - 1} \tag{15e}$$

or

$$C_l^m \left[\left(\frac{b}{c}\right)^{2l+1} \left(1 - \frac{\sigma_2}{\sigma_3}\right) - \left(1 + \frac{l}{l+1} \frac{\sigma_2}{\sigma_3}\right) \right] = D_l^m \left[b^{-(2l+1)} \left(1 - \frac{\sigma_2}{\sigma_3}\right) - c^{-(2l+1)} \left(1 + \frac{l+1}{l} \frac{\sigma_2}{\sigma_3}\right) \right] \tag{15f}$$

which we abbreviate as

$$\alpha C_l^m = \beta D_l^m. \tag{15g}$$

The boundary condition (14a) yields

$$\sigma_1 \left[A_l^m l a^{l-1} - K_l^m (l+1) \frac{1}{a^{l+2}} \right] = \sigma_2 C_l^m \left[l a^{l-1} - (l+1) \frac{\alpha}{\beta} a^{-(l+2)} \right] \tag{15h}$$

and the boundary conditon (14) is

$$A_l^m a^l + K_l^m \frac{1}{a^{l+1}} = C_l^m \left[a^l + \frac{\alpha}{\beta} a^{-(l+1)} \right]. \tag{15i}$$

By equating A_l^m from the above two equations we find

$$C_l^m = \frac{K_l^m (2l+1)}{l \left(1 - \frac{\sigma_2}{\sigma_1}\right) a^{2l+1} + \frac{\alpha}{\beta} \left(l + \frac{\sigma_2}{\sigma_1} (l+1) \right)} \tag{15j}$$

and

$$A_l^m = K_l^m \times \left(\frac{(2l+1)(\beta + \alpha a^{-(2l+1)})}{l \left(1 - \frac{\sigma_2}{\sigma_1}\right) \beta a^{2l+1} + \alpha \left(l + \frac{\sigma_2}{\sigma_1} (l+1) \right)} - a^{-(2l+1)} \right). \tag{15k}$$

Collectively, (15b), (15c), (15g), and (15j) result in

$$E_l^m = F_l^m \frac{l+1}{l} c^{-(2l+1)} = C_l^m \left(b^{2l+1} + \frac{\alpha}{\beta} \right) \frac{l+1}{l} \frac{c^{-(2l+1)}}{\frac{l+1}{l} \left(\frac{b}{c}\right)^{2l+1} + 1}. \tag{15l}$$

Based on this equation and (13b), we can calculate the potential on the scalp surface by

$$\Phi_3|_{r=c} = \sum_{l,m} \left[E_l^m \left(c^l + \frac{l}{l+1} c^{2l+1} c^{-(l+1)} \right) \right] S_l^m = \sum_{l,m} E_l^m c^l \frac{2l+1}{l+1} S_l^m. \tag{16}$$

And the potential in the brain $(r_0 < r \leq a)$ can be calculated by (10)–(13) and (15k). In particular, the potential on the cortical surface $(r = a)$ is

$$\Phi_1|_{r=a} = \sum_{l,m} \left[A_l^m a^l + K_l^m a^{-(l+1)} \right] S_l^m = \sum_{l,m} C_l^m \left(a^l + \frac{\alpha}{\beta} a^{-(l+1)} \right) S_l^m. \tag{17}$$

Considering a special case where $\sigma_1 = \sigma_3$ and the source is located on the z axis with $z = r_0$, the potential on the scalp

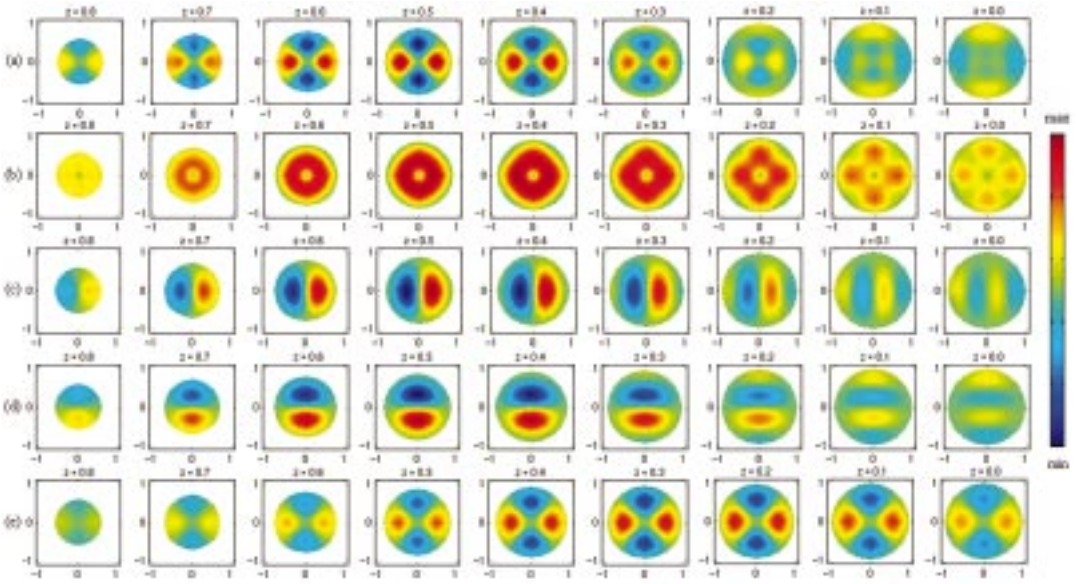

Fig. 3. The estimated equivalent source distributions corresponding to the source configuration illustrated in Fig. 2(a). (a) Equivalent current source density. (b) Moment of equivalent dipole sources. (c) The x component of equivalent dipole sources. (d) The y component of equivalent dipole sources. (e) The z component of equivalent dipole sources.

produced by a point current source located on the z axis can be represented by

$$\begin{aligned}\Phi_3|_{r=c} &= \sum_{l=1}^{\infty}\left[E_l\left(c^l + \frac{l}{l+1}c^{2l+1}c^{-(l+1)}\right)\right]P_l(\cos\theta)\\ &= \sum_{l=1}^{\infty}E_l c^l \frac{2l+1}{l+1}P_l(\cos\theta)\\ &= \sum_{l=1}^{\infty}\frac{Ir_0^l}{4\pi\sigma_3 c^{l+1}}\frac{s(2l+1)^3}{d_l(l+1)l}P_l(\cos\theta)\\ &= \sum_{l=1}^{\infty}\frac{If^l}{4\pi\sigma_3 c}\frac{s(2l+1)^3}{d_l(l+1)l}P_l(\cos\theta) \qquad (18)\end{aligned}$$

and the potential on the scalp produced by the z component P_z of a dipole located on the z axis is [27]

$$\begin{aligned}\Phi_3|_{r=c} &= \sum_{l=1}^{\infty}\frac{P_z l r_0^{l-1}}{4\pi\sigma_3 c^{l+1}}\frac{s(2l+1)^3}{d_l(l+1)l}P_l(\cos\theta)\\ &= \sum_{l=1}^{\infty}\frac{P_z l f^{l-1}}{4\pi\sigma_3 c^2}\frac{s(2l+1)^3}{d_l(l+1)l}P_l(\cos\theta) \qquad (19)\end{aligned}$$

where

$$\begin{aligned}s &= \frac{\sigma_2}{\sigma_1} = \frac{\sigma_2}{\sigma_3}\\ d_l &= ((l+1)s+l)\left(\frac{ls}{l+1}+1\right) + (1-s)((l+1)s+l)\\ &\quad\times\left(f_1^{l_1} - f_2^{l_1}\right) - l(1-s)^2\left(\frac{f_1}{f_2}\right)^{l_1},\\ l_1 &= 2l+1,\\ f_1 &= \frac{a}{c},\\ f_2 &= \frac{b}{c},\\ f &= \frac{r_0}{c}.\end{aligned}$$

The potential on the cortical surface $(r = a)$ produced by a point current source is

$$\begin{aligned}\Phi_1|_{r=a} &= \sum_{l=1}^{\infty}\frac{Ir_0^l}{4\pi\sigma_1 c^{l+1}}\frac{c_l}{d_l}P_l(\cos\theta)\\ &= \sum_{l=1}^{\infty}\frac{If^l}{4\pi\sigma_1 c}\frac{c_l}{d_l}P_l(\cos\theta) \qquad (20)\end{aligned}$$

and the potential on the cortical surface $(r = a)$ produced by a dipole is [27]

$$\begin{aligned}\Phi_1|_{r=a} &= \sum_{l=1}^{\infty}\frac{P_z l r_0^{l-1}}{4\pi\sigma_1 c^{l+1}}\frac{c_l}{d_l}P_l(\cos\theta)\\ &= \sum_{l=1}^{\infty}\frac{P_z l f^{l-1}}{4\pi\sigma_1 c^2}\frac{c_l}{d_l}P_l(\cos\theta) \qquad (21)\end{aligned}$$

where

$$\begin{aligned}c_l &= (2l+1)\left(f_1^l + \frac{\alpha}{\beta}f_1^{-(l+1)}\right),\\ d_l &= l(1-s)f_1^{2l+1} + \frac{\alpha}{\beta}(l+(1+l)s),\\ \alpha &= f_2^{2l+1}(1-s) - \left(1+\frac{ls}{1+l}\right),\\ \beta &= f_2^{-(2l+1)}(1-s) - \left(1+\frac{l+1}{l}s\right).\end{aligned}$$

IV. Results

A. Simulation Results

Fig. 3 shows an example of the ECS estimate and the EDS estimate for the four simulated radial dipoles as illustrated in

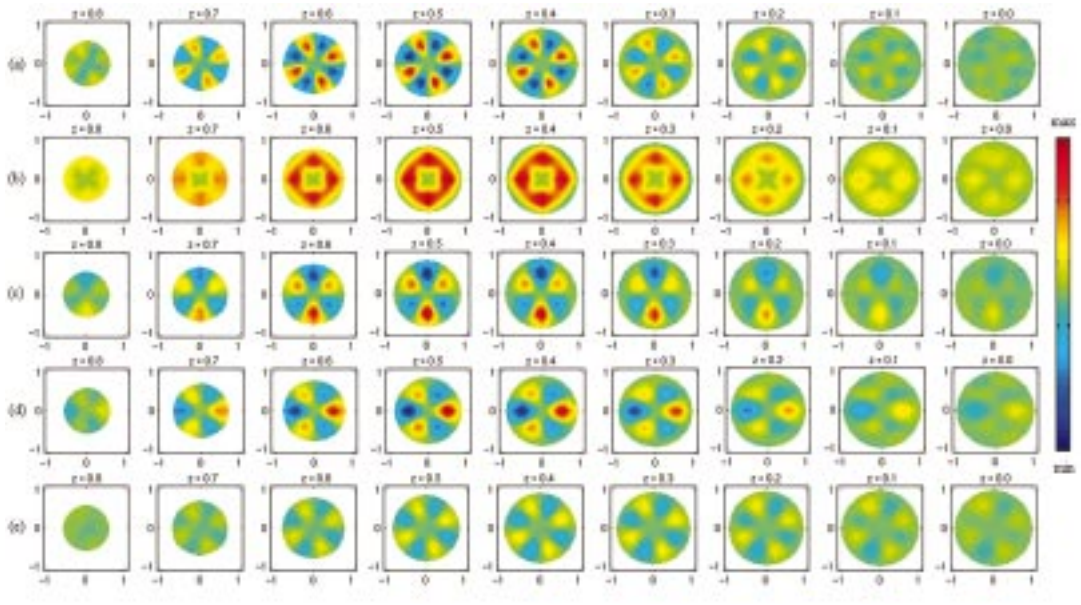

Fig. 4. The estimated equivalent source distributions corresponding to the source configuration illustrated in Fig. 2(b). (a) Equivalent current source density. (b) Moment of equivalent dipole sources. (c) The x component of equivalent dipole sources. (d) The y component of equivalent dipole sources. (e) The z component of equivalent dipole sources.

Fig. 2(a). The ECS imaging results are shown in Fig. 3(a). The EDS moment, x component, y component, and z component imaging results are shown in Fig. 3(b)–(e), respectively. The 64-level color scales, as shown by the color bar on the right of the figure, is used to illustrate the strength distribution of the inverse solution. The ECS strength and the EDS moment magnitude (nonnegative) are respectively normalized by their absolute maximum values. The three EDS directional components are normalized by the absolute maximum value of all three components, and the positive value indicates the component is along the $+x$ or $+y$ axis, while the negative value indicates the component is along the $-x$ or $-y$ axis.

Fig. 3(a) shows that the ECS estimate represents well four regions of activity close to the four source dipoles. The maximum source strength was estimated on layer $z = 0.5$ instead of $z = 0.4$. Such bias is a common phenomenon of the LWMN algorithm, not related to the ECS model. Since the two outward dipoles and two inward dipoles are all along radial direction, the sinks of the two outward dipoles gradually merge with the sources of the two inward dipoles at deeper layers like $z = 0.1$ and $z = 0.0$, where only few weak activities can be observed. Similarly, the EDS moment estimate shown in Fig. 3(b) illustrates a bias of shift of the maximum source magnitude somewhere between layers $z = 0.4$ and $z = 0.5$. While the EDS moment imaging suggests four source dipoles from its distribution at deep layers, its distribution at the layers close to the source dipoles ($z = 0.4$ and $z = 0.5$) is blurred because only magnitudes are depicted. To have a complete picture of the EDS distribution, the three EDS directional components are examined in Fig. 3(c)–(e). Clearly, the two outward radial dipoles located at $(\pm 0.4, 0, 0.4)$, respectively, show one $+x$ component and one $-x$ component at horizontal axis [Fig. 3(c)], while the two inward radial dipoles located at $(0, \pm 0.4, 0.4)$, respectively, show one $+y$ component and one $-y$ component at vertical axis [Fig. 3(d)]. All the four radial dipoles show components $+z$ or $-z$ direction depending on their outward/inward orientations [Fig. 3(e)]. The maximum strength of the estimated x component and y component appears between layers $z = 0.4$ and $z = 0.5$, while the z component reaches its maximum strength at layer $z = 0.3$.

Fig. 4 shows an example of the ECS imaging and the EDS imaging for four tangential dipoles as illustrated in Fig. 2(b). The method of display is the same as that in Fig. 3. Fig. 4(a) shows that the ECS estimate represents four pairs of source–sink distribution resolving the four source dipoles. The maximum source strength was estimated on layer $z = 0.5$ instead of $z = 0.4$, similar to the EDS moment distribution as illustrated in Fig. 4(b). Again, the orientation information of the dipole sources can be further revealed by examining the three EDS components' distribution as depicted in Fig. 4(c)–(e). The tangential dipole located at $(0, -0.4, 0.4)$ shows one $+x$ component, while the one located at (0, 0.4, 0.4) shows one $-x$ component [Fig. 4(c)]. Similarly, the two tangential dipoles located at $(\pm 0.4, 0, 0.4)$ show one $+y$ component and one $-y$ component, respectively [Fig. 4(d)]. Notably, Fig. 4(c) shows relatively weak "ghost" source in left and right, and Fig. 4(d) shows similar "ghost" source in top and bottom of the subplots. Interestingly, although actually there is no z component exists for the simulated dipole sources, Fig. 4(e) reveals relatively weak "ghost" components corresponding to the four tangential dipoles. The generation of these "ghost" sources may contribute to the intrinsic limitations of the MN or LWMN based inverse solutions [29]. While Fig. 4 demonstrates that the proposed ECS imaging is, in principle, *equivalent* to the EDS imaging approach, in that it provides source–sink distribution corresponding to the dipole sources, it also suggests its limitation, in cases like this, that additional information is needed to determine the current flows. Fig. 4 suggests that, in practice, a more complete picture on the 3-D neural current

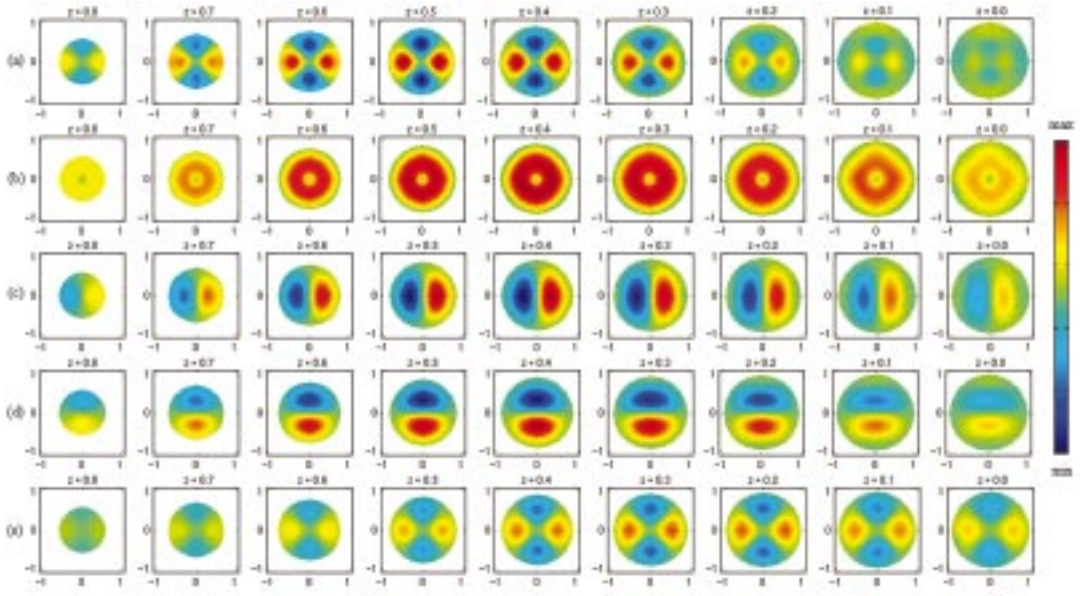

Fig. 5. The estimated equivalent source distributions corresponding to the source configuration illustrated in Fig. 2(c). (a) Equivalent current source density. (b)Moment of equivalent dipole sources. (c) The x component of equivalent dipole sources. (d) The y component of equivalent dipole sources. (e) The z component of equivalent dipole sources.

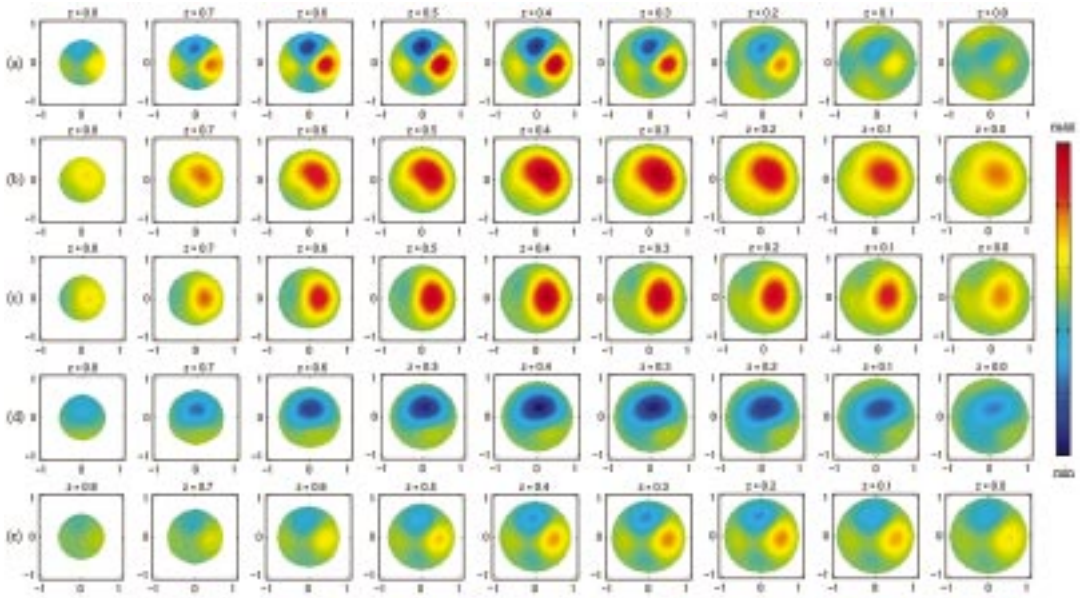

Fig. 6. The estimated equivalent source distributions corresponding to the source configuration illustrated in Fig. 2(d). (a) Equivalent current source density. (b) Moment of equivalent dipole sources. (c) The x component of equivalent dipole sources. (d) The y component of equivalent dipole sources. (e) The z component of equivalent dipole sources.

source distribution may be obtained by combining ECS and EDS estimates.

Fig. 5 shows an example of the ECS imaging and the EDS imaging for four current sources/sinks as illustrated in Fig. 2(c). Fig. 5(a) shows that the ECS estimate represents well the four areas of activity overlying the four sources/sinks. The information on the distribution of the current sources/sinks is well represented in the estimated ECS distribution. The maximum source strength was estimated somewhere between layers $z = 0.4$ and $z = 0.5$. Note that the EDS moment and three directional components' distributions shown in Fig. 5(b)–(e) are similar to those shown in Fig. 3(b)–(e), which correspond to four radial dipole sources. The current sources/sinks configuration in this example can be approximately represented by four tangential dipoles as illustrated by the dashed arrows shown in Fig. 2(c). Therefore, Fig. 5(c)–(d) reasonably shows the equivalent EDS components on x and y directions, while Fig. 5(e) shows the "ghost" EDS z component corresponding to the current sources/sinks.

Fig. 6 shows another example of the ECS imaging and the EDS imaging for a current source and a current sink as illustrated in Fig. 2(d). Fig. 6(a) shows that the ECS estimate represents well the source configuration consisting of a current source and a current sink, with the maximum estimated source strength located close to layer $z = 0.4$. The EDS moment distribution

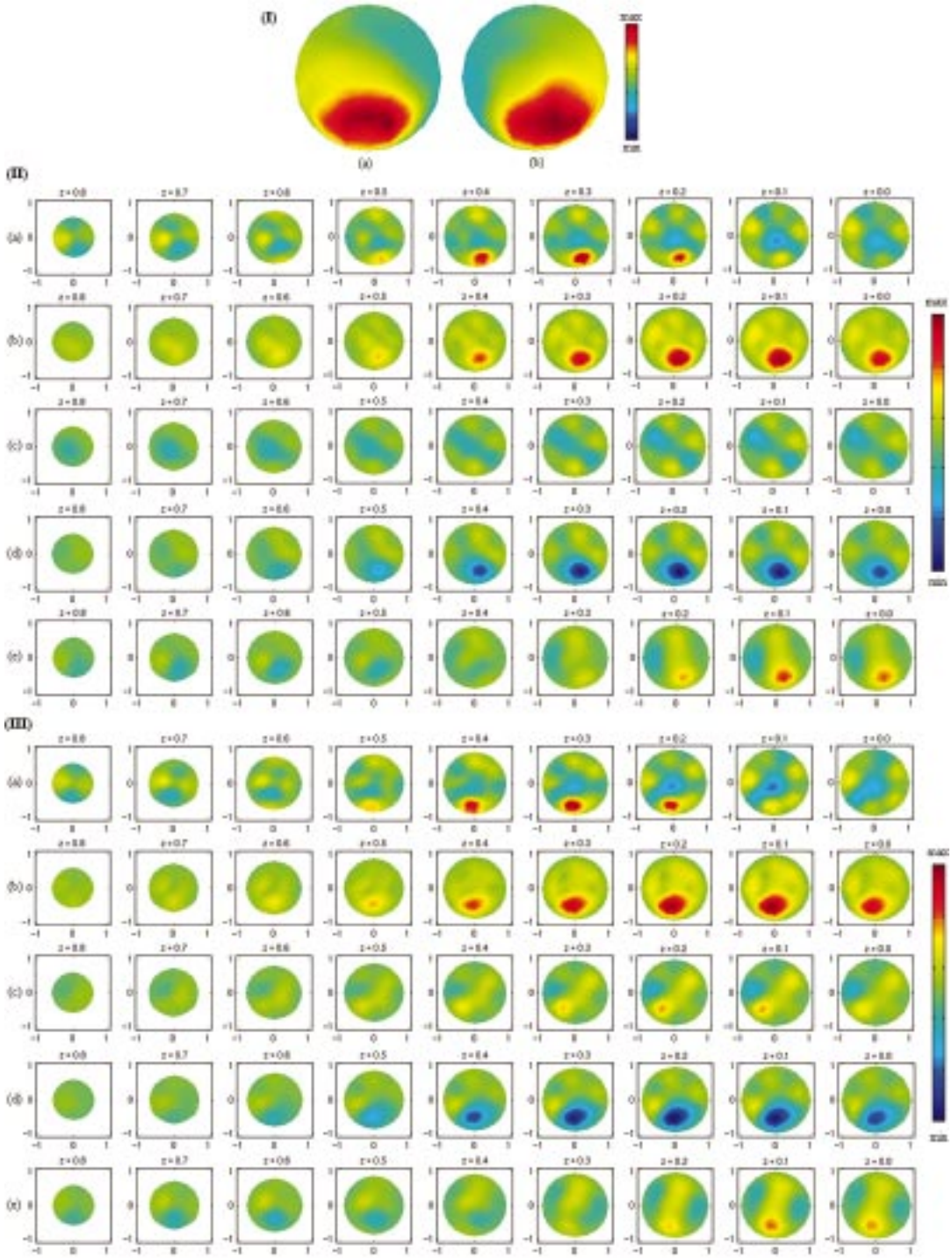

Fig. 7. (I) Top-back view of the scalp potential maps at P100 of VEP experiment. (a) Subject A was presented with the left visual field stimuli. (b) Subject B was presented with the right visual field stimuli. (See text for details.)(II) The estimated (a) ECS, (b) EDS moment, (c) EDS x component, (d) EDS y component, and (e) EDS z component distributions corresponding to the scalp potential map shown in Fig. 7(I-a). (III) The estimated (a) ECS, (b) EDS moment, (c) EDS x component, (d) EDS y component, and (e) EDS z component distributions corresponding to the scalp potential map shown in Fig. 7(I-b).

illustrates a single dipole approximately located at the center of the line connecting the source and the sink [Fig. 6(b)]. The orientation of this equivalent dipole can be approximately illustrated by the dashed arrow depicted in Fig. 2(d). Therefore, Fig. 6(c) and (d) reasonably shows the equivalent EDS components on x and y directions, while Fig. 6(e) shows the "ghost" EDS z component corresponding to the current source/sink.

B. Human VEP Experimental Results

The pattern reversal VEP data at the P100 were analyzed by using both ECS and EDS imaging approaches. Two representative examples are given below as illustrations. Subject A was presented with the left visual field stimuli, and Fig. 7(I-a) displays the top-back view of the scalp potential map at P100,

which shows a dominant positive potential component symmetrically distributed over the occipital area of the scalp. On the other hand, subject B was presented with the right visual field stimuli, and the top-back view of the recorded scalp potential map at P100 is shown in Fig. 7(I-b), which can be characterized by a widely distributed positive potential component on the right scalp.

For the P100 scalp potential map elicited by the left visual field stimuli in Subject A, Fig. 7(II-a) and (II-b), respectively, shows the ECS distribution and the EDS moment distribution, while the x, y, and z component distributions of the EDS estimate are illustrated in Fig. 7(II-c)–(III-e), respectively. The ECS estimate shows the maximum strength source at layer $z = 0.3$, located on the right occipital area of the brain close to the right visual cortex. The estimated strongest sink lies at layer $z = 0.1$, located at a more medial and deeper position as compared with the maximum strength source position. The EDS moment distribution shows strongest activity between layers $z = 0.1$ and $z = 0.2$, in the position close to the right visual cortex. The estimated directional EDS components show dominant activity along $-y$ direction between layers $z = 0.1$ and $z = 0.3$, and apparent activity along $+z$ direction around layer $z = 0.1$, and all these activities are located close to the right visual cortex. Clearly, the source/sink distribution estimated by the ECS imaging approach suggests a current flow pathway consistent with the EDS imaging results.

For the P100 scalp potential map elicited by the right visual field stimuli in Subject B, Fig. 7(III-a) and (III-b), respectively, shows the ECS distribution and the EDS moment distribution, while the three directional EDS component distributions are illustrated in Fig. 7(III-c)–(III-e), respectively. The ECS estimate shows the maximum strength source at layer $z = 0.3$, located on the left occipital brain area close to the left visual cortex. The estimated sink has strongest strength at layer $z = 0.1$, located at a more medial and deeper position, with a little extension to the left occipital area of the brain. The EDS moment estimate shows strongest magnitude between layers $z = 0.1$ and $z = 0.2$, in the position close to the left visual cortex. The estimated directional EDS components show dominant activity along $-y$ direction between layers $z = 0.1$ and $z = 0.3$. Apparent activity along $+z$ direction around layer $z = 0.1$ and some activity along $+x$ direction between layers $z = 0.1$ and $z = 0.2$ can also be observed, and all these estimated EDS components are located close to the left visual cortex. Again, the source/sink distribution estimated by the ECS imaging approach suggests a current flow pathway consistent with the EDS imaging results.

V. Discussion

Bioelectrical sources have been estimated by using a number of equivalent source models, in particular, the equivalent dipole models. The wide use of equivalent dipole models is partially due to the fact that the dipole represents well a localized area of neural activity inside the brain. On the other hand, it has been shown that both the equivalent volume current source (monopole) and the equivalent volume dipole source (dipole) can equivalently represent the bioelectric sources originating from neuronal membrane excitation [20], [45]–[48]. The equivalent monopole source models have been previously used in investigations on equivalent surface sources [30]–[32]. The equivalent 3-D current source modeling, which we have been pursuing in our laboratory at the University of Illinois [13], represents a further effort toward modeling of bioelectric sources. Since the three-concentric-sphere inhomogeneous model has been widely used as a reasonable approximation of the head volume conductor, our theoretical work in developing the closed form solution of the scalp potentials due to a point current source provides not only a basic forward solution for the proposed ECS imaging, but also a solution which would be useful to researchers for other work involving modeling and imaging of brain electric sources.

Imaging of brain electrical activity has received significant attention in the past decades. A number of techniques have been developed for estimating and imaging electric activity in the brain from noninvasive electrical or magnetic measurements. Dipole localization techniques have been used for localizing one or few well-localized brain sources [3]–[5]. Scalp Laplacian mapping techniques have been used to enhance the spatial resolution of the scalp potential maps for estimating the cortical electrical activity [2], [33]–[36]. Cortical imaging has been developed to de-convolve the smoothing effect of the head volume conductor, providing estimation of cortical electrical activity [2], [13], [35], [37]–[43]. Recently, 3-D imaging techniques have been further developed to estimate the distribution of electrical sources throughout the neuronal tissue in the brain [9]–[18], [46], including reconstruction of equivalent dipole distribution or electrical potentials in the 3-D volume.

In the present study, we have developed a new approach to estimate the 3-D equivalent current source distribution from scalp EEG. We have realized the inverse estimation by using the LWMN algorithm, while other inverse algorithms may be used in equivalent current source imaging. The present computer simulation results clearly demonstrate the efficacy of the ECS approach in imaging the distribution of equivalent current sources in the brain. For both the dipole sources and the point current sources, the ECS imaging approach can resolve the source configuration to the degree of the spatial resolution as allowed by the LWMN algorithm. The limited spatial resolution of the LWMN algorithm is due to the constraint inherited to minimize the Laplacian of the source distribution, thus, effectively removing the high spatial frequency components. Such operation is to ensure the reconstruction of a unique solution for the highly underdetermined inverse problem. The limitation of the MN or WMN algorithms has been addressed by several investigators [9], [15], [40] and is beyond the scope of the present paper. Although we only used the LWMN algorithm in the present study to implement the inverse estimation, other inverse estimation techniques (for example, the inverse estimators provided in [14]–[18]) can also be used to implement the equivalent current source imaging.

It is noteworthy that the ECS imaging results are consistent with those obtained by using the EDS imaging approach,

in that the ECS imaging provides important information on the source–sink configuration of the "actual" sources (see Figs. 3–6). Theoretically speaking, either the equivalent dipole source model or the equivalent current source model should be able to represent the electrical source distribution. While the EDS imaging can also reveal the direction information of the dipole sources, by simultaneously displaying its x, y, and z component distributions, the ECS imaging approach reduces the solution space to one third of that of the EDS imaging approach, thus, substantially improves the computational efficiency. Our simulation studies have demonstrated that the EDS moment estimate only reveals the dipole intensity distribution without orientation information, which should be retrieved by examining the EDS component distribution in three dimensions. The ECS estimate, however, can effectively reconstruct the source/sink configuration, which may suggest the orientation of the source dipoles, or the pathway of the current flows in the brain.

The present 3-D brain electric source imaging technique was also applied to the VEP data analysis, and consistent results were obtained from both ECS and EDS imaging approaches (Fig. 7). It is widely accepted that the half visual field stimuli activate the visual cortex on the contralateral hemisphere of the brain. But paradoxically, the half visual field stimuli elicited stronger positive potential distribution over the midline or ipsilateral side of the scalp. However, both the ECS estimate and the EDS estimate clearly indicate that the contralateral visual cortex was activated [44], thus, effectively eliminated the misleading far field observed in the scalp potential. Consistent with the simulation study, the ECS estimate of the source/sink distribution underlying the scalp VEP measurement gave almost equivalent information on the source location and orientation information as those revealed by the EDS estimate.

In summary, the simulation and experimental studies have demonstrated the excellent performance of the ECS estimate in imaging brain electrical sources. The ECS imaging approach gives consistent results as the EDS imaging approach, but is much more computationally efficient. The ECS imaging approach may become an important alternative to imaging of bioelectric sources in the brain and other organ systems.

ACKNOWLEDGMENT

The authors are grateful to anonymous reviewers for their constructive comments to the previous version of the manuscript.

REFERENCES

[1] A. Gevins, "The future of electroencephalography in assessing neurocognitive functioning," *Electroenceph. Clin. Neurophysiol.*, vol. 106, pp. 165–172, 1998.

[2] B. He, "Brain electric source imaging: Scalp Laplacian mapping and cortical imaging," *Crit. Rev. Biomed. Eng.*, vol. 27, pp. 149–188, 1999.

[3] M. Scherg and D. von Cramon, "Two bilateral sources of the late AEP as identified by a spatio-temporal dipole model," *Electroenceph. Clin. Neurophysiol.*, vol. 62, pp. 32–44, 1985.

[4] B. He, T. Musha, Y. Okamoto, S. Homma, Y. Nakajima, and T. Sato, "Electric dipole tracing in the brain by means of the boundary element method and its accuracy," *IEEE Trans. Biomed. Eng.*, vol. BME–34, pp. 406–414, 1987.

[5] B. N. Cuffin, "EEG dipole source localization," *IEEE Eng. Med. Biol. Mag.*, vol. 17, pp. 118–122, 1998.

[6] J. C. Mosher, P. S. Lewis, and R. M. Leahy, "Multiple dipole modeling and localization from spatio-temporal MEG data," *IEEE Trans. Biomed. Eng.*, vol. 39, pp. 541–557, 1992.

[7] M. S. Hamalainen and R. Ilmoniemi, "Interpreting measured magnetic fields of the brain: Estimates of current distributions," Helsinki Univ. Technol, Helsinki, Finland, Tech. Rep. TKF-F-A559, 1984.

[8] B. Jeffs, R. Leahy, and M. Singh, "An evaluation of methods for neuromagnetic image reconstruction," *IEEE Trans. Biomed. Eng.*, vol. BME–34, pp. 713–723, 1987.

[9] I. F. Gorodnitsky, J. S. George, and B. D. Rao, "Neuromagnetic source imaging with FOCUSS: A recursive weighted minimum norm algorithm," *Electroenceph. Clin. Neurophysiol.*, vol. 95, pp. 231–251, 1995.

[10] R. D. Pascual-Marqui, C. M. Michel, and D. Lehmann, "Low resolution electromagnetic tomography: A new method for localizing electrical activity in the brain," *Int. J. Psychophysiol.*, vol. 18, pp. 49–65, 1994.

[11] R. D. Pascual-Marqui, "Reply to comments by Hämäläinen, Ilmoniemi, and Nunez," *ISBET Newslett.*, no. 6, pp. 16–28, 1995.

[12] G. Lantz, C. M. Michel, R. D. Pascual-Marqui, L. Spinelli, M. Seeck, S. Seri, T. Landis, and I. Rosen, "Extracranial localization of intracranial interictal epileptiform activity using LORETA (low resolution electromagnetic tomography)," *Electroenceph. Clin. Neurophysiol.*, vol. 102, pp. 414–422, 1997.

[13] D. Yao and B. He, "The Laplacian weighted minimum norm estimate of three dimensional equivalent charge distribution in the brain," in *Proc. Annu. Int. Conf. IEEE Engineering in Medicine and Biology Society*, 1998, pp. 2108–2111.

[14] S. Baillet and L. Garnero, "A Bayesian approach to introducing anatomo-functional priors in the EEG/MEG inverse problem," *IEEE Trans. Biomed. Eng.*, vol. 44, pp. 374–385, May 1997.

[15] J. W. Phillips, R. M. Leahy, and J. C. Mosher, "MEG-based imaging of focal neuronal current sources," *IEEE Trans. Med. Imag.*, vol. 16, pp. 338–348, June 1997.

[16] K. Sekihara and B. Scholz, "Average-intensity reconstruction and Wiener reconstruction of bioelectric current distribution based on its estimated covariance matrix," *IEEE Trans. Biomed. Eng.*, vol. 42, pp. 149–157, Feb. 1995.

[17] B. Van Veen, W. van Drongelen, M. Yuchtman, and A. Suzuki, "Localization of brain electrical activity via linearly constrained minimum variance spatial filtering," *IEEE Trans. Biomed. Eng.*, vol. 44, pp. 867–880, Sept. 1997.

[18] M. Fuchs, M. Wagner, T. Kohler, and H. A. Wischmann, "Linear and nonliner current density reconstructions," *J. Clin. Neurophysiol.*, vol. 16, pp. 267–295, 1999.

[19] A. S. Ferguson and D. Durand, "A theory of the magnetic field from current monopoles," *J. Appl. Phys.*, vol. 71, pp. 3107–3113, 1992.

[20] R. Plonsey, *Bioelectric Phenomena*. New York: McGraw-Hill, 1969.

[21] J. A. Stratton, *Electromagnetic Theory*. New York: McGraw-Hill, 1941.

[22] J. Z. Wang, S. J. Williamson, and L. Kaufman, "Magnetic source images determined by a least-field analysis: The unique minimum-norm least-squares estimation," *IEEE Trans. Biomed. Eng.*, vol. 39, pp. 665–675, July 1992.

[23] P. C. Hansen, "Analysis of discrete ill-posed problems by means of the L-curve," *SIAM Rev.*, vol. 34, pp. 561–580, 1992.

[24] V. A. Morozov, "Choice of parameter for the solution of functional equations by the regularization method," *Sov. Math. Doklady*, vol. 8, pp. 1000–1003, 1967.

[25] S. Rush and D. A. Driscoll, "EEG electrode sensitivity—An application of reciprocity," *IEEE Trans. Biomed. Eng.*, vol. BME–16, pp. 15–22, 1969.

[26] R. N. Kavanagh, T. M. Darcey, D. Lehmann, and D. H. Fender, "Evaluation of methods for three-dimensional localization of electrical sources in the human brain," *IEEE Trans. Biomed. Eng.*, vol. BME–25, pp. 421–429, 1978.

[27] Y. Eshel, "Correlations Between Anatomical Asymmetries in the Head and Scalp Potential Amplitude Asymmetry—A mathematical Model," Ph.D. dissertation, Tel-Aviv Univ., Tel-Aviv, Israel, 1993.

[28] E. W. Hobson, *The Theory of Spherical and Ellipsoidal Harmonics*. Cambridge, U.K.: Cambridge Univ. Press, 1931.

[29] M. Hamalainen, "Discrete and distributed source estimates," *ISBET Newslett.*, no. 6, pp. 9–12, 1995.

[30] B. He and R. J. Cohen, "Body surface Laplacian ECG mapping," *IEEE Trans. Biomed. Eng.*, vol. 39, pp. 1179–1191, Nov. 1992.
[31] B. He, Y. B. Chernyak, and R. J. Cohen, "An equivalent body surface charge model representative three-dimensional bioelectrical activity," *IEEE Trans. Biomed. Eng.*, vol. 42, pp. 637–646, July 1995.
[32] D. Yao, "The equivalent source technique and cortical imaging," *Electroenceph. Clin. Neurophysiol.*, vol. 98, pp. 478–483, 1996.
[33] B. Hjorth, "An on-line transformation of EEG scalp potentials into orthogonal source derivations," *Electroenceph. Clin. Neurophysiol.*, vol. 39, pp. 526–530, 1975.
[34] F. Perrin, O. Bertrand, and J. Pernier, "Scalp current density mapping: Value and estimation from potential data," *IEEE Trans. Biomed. Eng.*, vol. BME–34, pp. 283–288, 1987.
[35] P. Nunez, R. B. Silibertein, P. J. Cdush, R. S. Wijesinghe, A. F. Westdrop, and R. Srinivasan, "A theoretical and experimental study of high resolution EEG based on surface Laplacian and cortical imaging," *Electroenceph. Clin. Neurophysiol.*, vol. 90, pp. 40–57, 1994.
[36] F. Babiloni, C. Babiloni, F. Carducci, L. Fattorini, P. Onorati, and A. Urbano, "Spline Laplacian estimate of EEG potentials over a realistic magnetic resonance-constructed scalp surface model," *Electroenceph. Clin. Neurophysiol.*, vol. 98, pp. 363–373, 1996.
[37] R. Sidman, M. Ford, G. Ramsey, and C. Schlichting, "Age-related features of the resting and P300 auditory evoked responses using the dipole localization method and cortical imaging technique," *J. Neurosci. Meth.*, vol. 33, pp. 23–32, 1990.
[38] A. Gevins, J. Le, N. K. Martin, P. Brickett, J. Desmond, and B. Reutter, "High resolution EEG: 124-channel recording, spatial deblurring and MRI integration methods," *Electroenceph. Clin. Neurophysiol.*, vol. 90, pp. 337–358, 1994.
[39] F. Babiloni, C. Babiloni, F. Carducci, L. Fattorini, C. Anello, P. Onorati, and A. Urbano, "High resolution EEG: A new model-dependent spatial deblurring method using a realistically-shaped MR-constructed subject's head model," *Electroenceph. Clin. Neurophysiol.*, vol. 102, pp. 69–80, 1997.
[40] R. Srebro, "Estimating cortical activity from VEP's with the shrinking ellipsoid inverse," *Electroenceph. Clin. Neurophysiol.*, vol. 102, pp. 343–355, 1997.
[41] Y. Wang and B. He, "A computer simulation study of cortical imaging from scalp potentials," *IEEE Trans. Biomed. Eng.*, vol. 45, pp. 724–735, June 1998.
[42] B. He, Y. Wang, and D. Wu, "Estimating cortical potentials from scalp EEGs in a realistically shaped inhomogeneous head model," *IEEE Trans. Biomed. Eng.*, vol. 46, pp. 1264–1268, Oct. 1999.
[43] B. He, J. Lian, K. M. Spencer, J. Dien, and E. Donchin, "A cortical potential imaging analysis of the P300 and novelty P3 components," *Human Brain Map.*, vol. 12, pp. 120–130, 2001.
[44] G. Barrett, L. Blumhardt, A. M. Halliday, E. Halliday, and A. Kriss, "A paradox in the lateralization of the visual evoked response," *Nature*, vol. 261, pp. 253–255, 1976.
[45] B. He, D. Yao, and D. Wu, "Imaging brain electrical activity," in *Advances in Electromagnetic Fields in Living Systems*, J. C. Lin, Ed. New York: Plenum, 2000, vol. 3, pp. 73–120.
[46] R. Grave de Peralta, S. Gonzalez, S. Morand, C. Michel, and T. Landis, "Imaging the electrical activity of the brain: ELECTRA," *Human Brain Map.*, vol. 9, pp. 1–12, 2000.
[47] J. Malmivuo and R. Plonsey, *Bioelectromagnetism*. New York: Oxford Univ. Press, 1995.
[48] R. M. Gulrajani, *Bioelectricity and Biomagnetism*. New York: Wiley, 1998.

Bin He (S'87–M'88–SM'97) received the Ph.D. degree in bioelectrical engineering with the highest honors from the Tokyo Institute of Technology, Tokyo, Japan and completed the postdoctoral fellowship in biomedical engineering at Harvard University—MIT, Cambridge.

After working as a Research Scientist at Massacxhusetts Institute of Technology (M.I.T.), He joined the faculty of the University of Illinois at Chicago. He is currently an Associate Professor of Bioengineering and of Electrical and Computer Engineering and the Director of Biomedical Functional Imaging and Computation Laboratory. His major research interests include modeling and imaging of bioelectric activity, neural engineering, cardiovascular engineering, and computational biomedicine.

Dr. He is the recipient of an NSF CAREER Award, the UIC College of Engineering Faculty Research Award, and the American Heart Association Established Investigator Award. He has been named a University Scholar by the President of the University of Illinois.

D. Yao received the Ph.D. degree in applied geophysics from Chengdu University of Technology, Chengdu, China, in 1991.

He has been on the faculty of the University of Electronic Science and Technology of China. He had been a Visiting Scholar in the Biomedical Functional Imaging and Computation Laboratory at the University of Illinois at Chicago from September 1997 to August 1998, and a Visiting Professor at McMaster University, Hamilton, QC, Canada, from November 2000 to May 2001. He is the author of more than 80 scientific papers. His current interests are in the source analysis of bioelectromagnetic measurements, high-resolution EEG mapping, spatio-temporal dynamics of neural electric activities, fMRI, and information technology in medical physics.

Jie Lian (S'97) received the B.S. and M.S. degrees in biomedical engineering from Zhejiang University, Hangzhou, China, in 1992 and 1995, respectively. After working as a research associate at Zhejiang University for two years, he has been working toward the Ph.D. degree in Department of Bioengineering at the University of Illinois at Chicago. His dissertation research is focused on high-resolution imaging of brain and cardiac electrical activity from EEG and ECG measurement.

He has research background in biological signal processing and analysis, algorithm development and computer simulation, human experimentation, and biomedical instrumentation.

D. Wu received the B.S. and M.S. degrees in electrical engineering from Tsinghua University, Beijing, China, in 1992 and 1994, respectively, and the Ph.D. degree in bioengineering from the University of Illinois at Chicago, in 1998. Her doctoral dissertation concerned the forward and inverse problems of electrocardiography.

She is currently with Morningstar, Inc., Chicago, IL.